Biosensors and Bioelectronics 177 (2021) 112949

Contents lists available at ScienceDirect

Biosensors and Bioelectronics

journal homepage: http://www.elsevier.com/locate/bios

Faradaic electrochemical impedance spectroscopy for enhanced analyte detection in diagnostics

Madison E. Strong, Jeffrey R. Richards, Manuel Torres, Connor M. Beck, Jeffrey T. La Belle *

College of Engineering, Science, and Technology, Grand Canyon University, Phoenix, AZ, USA

ARTICLE INFO

Keywords:
Electrochemical impedance spectroscopy
Surface modifications
Multimarker
Continuous
Molecular recognition element
Faradaic

ABSTRACT

Electrochemical impedance spectroscopy (EIS) is a widely implementable technique that can be applied to many fields, ranging from disease detection to environmental monitoring. EIS as a biosensing tool allows detection of a broad range of target analytes in point-of-care (POC) and continuous applications. The technique is highly suitable for multimarker detection due to its ability to produce specific frequency responses depending on the target analyte and molecular recognition element (MRE) combination. EIS biosensor development has shown promising results for the medical industry in terms of diagnosis and prognosis for various biomarkers. EIS sensors offer a cost-efficient system and rapid detection times using minimal amounts of sample volumes, while simultaneously not disturbing the sample being studied due to low amplitude perturbations. These properties make the technique highly sensitive and specific. This paper presents a review of EIS biosensing advancements and introduces different detection techniques and MREs. Additionally, EIS's underlying theory and potential surface modification techniques are presented to further demonstrate the technique's ability to produce stable, specific, and sensitive biosensors.

1. Introduction

Biosensor development for use in an array of applications is a rapidly growing field. Possible utilization includes disease detection and monitoring, drug discovery, water quality management, and environmental monitoring. These analytical devices can detect many substances, also called analytes, and combine biological and physiochemical detection components. Analytes refer to the substance of interest whose concentration is quantified through signals generated from chemical interactions taking place on the sensor. Due to the wide variety of detectable analytes and the multifaceted nature of biosensing, there are many factors to consider when determining the best type of biosensing platform for a desired application. This includes the type of molecular recognition element, which is differentiated by type of bioreceptors for an analyte (i.e. enzymes and antibodies), along with the sensing modality (i.e. optical, mechanical, and electrochemical), and base/electrode material. The applications and usefulness of these sensors are characterized through their sensitivity, reproducibility, stability, selectivity, and linearity (Bhalla et al., 2016).

More specifically, electrochemical impedance spectroscopy (EIS) applications as a sub-class of electrochemical sensing modalities are advancing rapidly, especially for diagnostics. This is due to their ability to identify analyte concentrations at a faster rate than traditional laboratory practices and provide large amounts of useable measurements. EIS also minimizes destruction and alterations to the biological media because of small signal application, while possessing linearity along with thermal and temporal stability (Ramírez et al., 2009). Impedimetric biosensors are capable of operating without additional analyte tagging, such as the attachment of a fluorescent probe in ELISA testing. Impedimetric biosensors are nondestructive and provide a rapid sensing method with small sample volumes (~<20 μL). They also use specific molecular recognition elements, such as antibodies, RNA, DNA, and aptamers to provide highly selective and sensitive analyte testing (Randviir and Banks, 2013). Fig. 1 demonstrates EIS applications across different fields. EIS principles will be explained briefly, followed by novel advancements completed in the EIS field of biosensing over the last 5 years.

2. Electrochemical Impedance Spectroscopy Principles and Fundamentals

EIS is a technique used to analyze the electrical response of a cell to

* Corresponding author. College of Engineering, Science, and Technology, Grand Canyon University, Phoenix, AZ, USA.
E-mail addresses: jeff.labelle@gcu.edu, jeff@labellelabs.com (J.T. La Belle).

https://doi.org/10.1016/j.bios.2020.112949
Received 30 May 2020; Received in revised form 13 December 2020; Accepted 24 December 2020
Available online 31 December 2020

an applied potential throughout numerous frequencies, capable of being performed in both faradaic and non-faradaic settings (Lin et al., 2017). EIS can be utilized for biological applications by targeting the analyte through a composite set on the electrode surface. This technique impacts the conductivity of the system by either a blocking mechanism or an admittance mechanism (Randviir and Banks, 2013). The implementation of coatings can vary polarization resistance, whereas selecting a catalyst coat will reduce polarization resistance and increase capacitance (He and Mansfeld, 2009). Beyond the biosensing field, EIS can be used to visualize the deterioration of a coating prior to visible defects being revealed. Some EIS techniques to test coating include exposure tests, as well as immersion and impedance measurements, which give insight on electrode deterioration over time (Loveday et al., 2004).

Impedimetric biosensors function by measuring the complex form of resistance, known as impedance. While resistance takes place in direct current (DC) circuits where there is no current directional alteration and obeys Ohm's law, impedance occurs in an alternating current (AC) circuit where AC voltage and current are out of phase with each other. These AC signals follow a sinusoidal wave occurring at different frequencies and can create frequency dependent effects. This is caused by differences in phase angles (θ) which produce a capacitive and/or inductive effect at almost all frequencies, as well as a change to the complex impedance ($|Z|$) of the system (Leva-Bueno et al., 2020; Randviir and Banks, 2013). This phase angle can be significant at low frequencies due to a limitation of electron-transfer processes from the mass transport of an electroactive species (Randviir and Banks, 2013). Phase angle is the difference between voltage and current phase, while complex impedance is the difference between voltage and current amplitudes. Complex impedance is broken into its resistive (Z') and capacitive ($-Z''$) portions, also known as real and imaginary impedance, respectively. The resistive portion stems from opposing current flow by the electrode surface, while the capacitive portion shows the charge storage in the system from the applied potential. This results in impedance being defined as a complex resistance encountered when current flows through a circuit containing resistors, capacitors, or inductors (Leva-Bueno et al., 2020; Park and Yoo, 2003).

EIS uses a small fixed sinusoidal voltage generally applied on a three-electrode cell containing an electrolyte solution with the analyte being investigated (Randviir and Banks, 2013). A three-electrode cell is composed of a working, counter, and reference electrode, where working, counter, and reference leads connect to their respective electrodes. These electrodes are made out of a wide variety of materials (carbon, gold, platinum, etc.), depending on the specific application. When an AC potential is applied to the cell, current is carried between the counter and working electrodes, and potential is monitored by the working and reference electrodes (Waleed Shinwari et al., 2010). A faradaic process occurs at the working electrode by a redox mechanism (commonly a redox probe/electron mediator) following Faraday's law, whereas a non-faradaic process takes place at the working electrode without any charge transfer. Regardless of its inability to transfer charge, the capacitive nature of the system still allows electricity to flow through the electrode (Leva-Bueno et al., 2020). In faradaic methods, impedance can be measured by adding a redox probe, such as potassium ferricyanide or potassium ferrocyanide, to the electrode surface containing the analyte

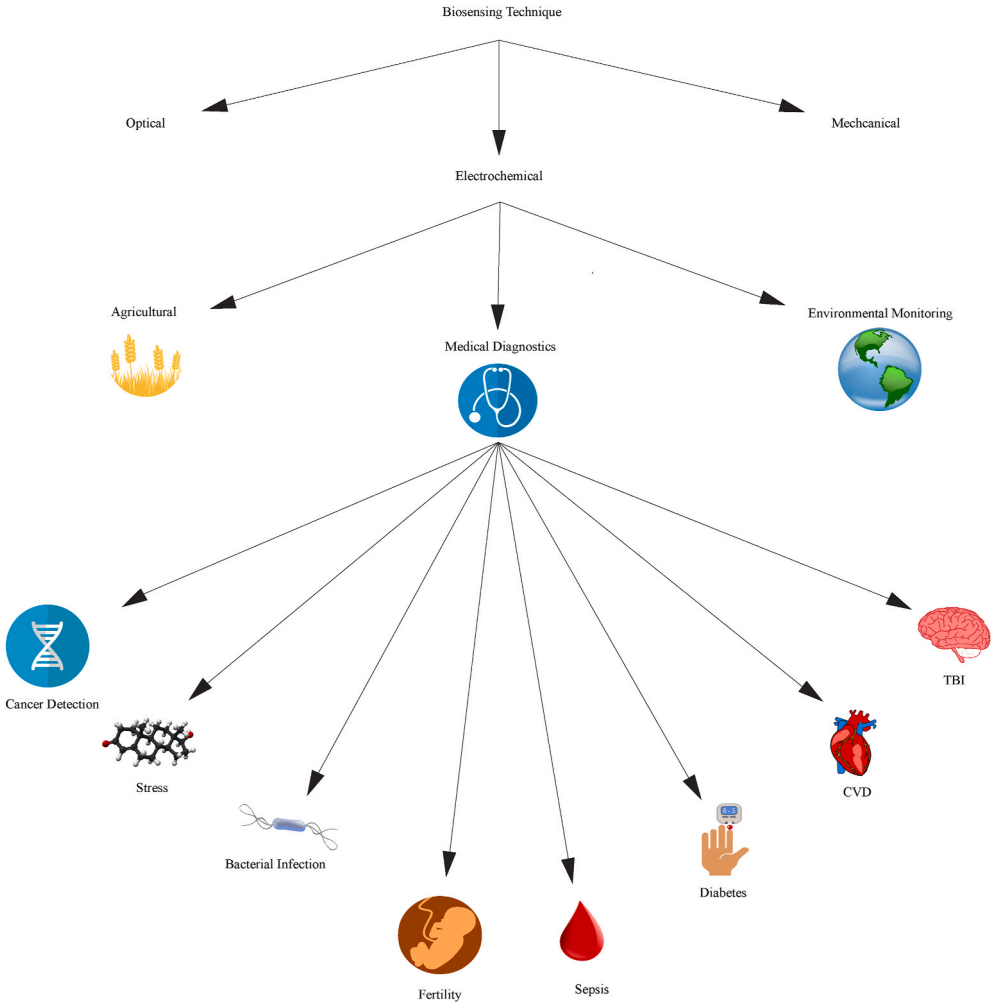

Fig. 1. Diagram showing broad EIS applications.

and composite. The potential load allows current to flow through the system and converts it into complex impedance through a potentiostat. This process is reproduced through various frequencies, observing real and imaginary values for the overall impedance (Randviir and Banks, 2013).

What we know as EIS today has come a long way since the groundwork was laid in the 1880's. Oliver Heaviside defined impedance and created several operation transformations, such as the $s = d/dt$ and $1/s = \int dt$ Laplace transforms and $s = j\omega$, which allowed the Laplace domain to be transformed to the Fourier domain (MacDonald, 2006). Equation (1) denotes operational impedance as derived by Oliver Heaviside, where Z is impedance, V is the voltage, I is the current, j is the imaginary component, and ω is the frequency (Leva-Bueno et al., 2020; Randviir and Banks, 2013).

$$Z(j\omega) = \frac{V(j\omega)}{I(j\omega)} \tag{1}$$

The technology has continued to advance since the 1880's, with notable developments. Walther Nersnt began to apply EIS techniques toward dielectrics in 1894, which contributed to the implementation of Warburg's diffusion to EIS applications (Nara et al., 2020). Warburg's diffusion came from his 1899 work which detailed the impedance of diffusional transport between an electroactive species and electrode surface. Early equivalent circuit modeling was tested by Dolin and Ershler in 1940 by interpreting an electrochemical reaction's impedance response. This led to the implementation of the Randles circuit for EIS by J.E.B. Randles in 1947, as well as mixed kinetic and diffusion models and corrosion models for failed coatings further down the road (MacDonald, 2006; Nara et al., 2020). The Randles circuit is the most commonly used circuit to model EIS data, composed of a solution resistance in series with a parallel mixture of charge transfer resistance and double-layer capacitance. It can be modified with a Warburg's diffusional element to represent bulk solution properties (Honikel et al., 2018). In the Warburg diffusion element, a species in the solution diffuses either away or toward an electrode-electrolyte interface caused by a redox reaction (Huang, 2018). Warburg diffusion is significant at low frequencies because of electroactive species limiting the electron transfer process (Leva-Bueno et al., 2020; Park and Yoo, 2003).

Equations (2) and (3) show real and imaginary impedances usually displayed in a Nyquist plot from EIS. The variable R_s is solution resistance, R_{ct} is charge transfer resistance, ω is angular frequency, and c_{dl} is double layer capacitance (Leva-Bueno et al., 2020; Randviir and Banks, 2013).

$$Z' = R_s + \frac{R_{ct}}{1 + \omega^2 R_{ct}^2 C_{dl}^2} \tag{2}$$

$$Z'' = \frac{R_{ct}^2 C_{dl} \omega}{1 + \omega^2 R_{ct}^2 C_{dl}^2} \tag{3}$$

Fig. 2 demonstrates a simple interaction between components needed to create an EIS system, comprised of a potentiostat, sensor platform, and computer software. From Fig. 2, (A) displays the Nyquist plot and (B) displays the Bode plot obtained during the EIS process. The Nyquist plot in (A) contains real impedance (x-axis) and imaginary impedance (y-axis) at different frequencies. The Bode plot in (B) represents the respective logarithmic frequency (x-axis) plotted against the logarithmic complex impedance and phase angle (y-axis). In a Nyquist plot, Warburg diffusion can generally be identified as a straight line with a phase angle of 45° (He and Mansfeld, 2009; Leva-Bueno et al., 2020; Park and Yoo, 2003).

Currently, EIS technology continues to develop and is used in a multitude of fields, but the application to biosensing has advanced steadily due to rapid result times and high sensitivity. Interactions between MRE's and analytes have been documented to have an optimal binding frequency (OBF) for EIS, where a change in an analytes concentration correlates strongly to an impedance reading at a specific frequency (Haselwood and la Belle, 2015; Lin et al., 2017; Malkoc et al., 2017). The technique also boasts low production costs, point-of-care (POC) and continuous capabilities, low limits of detection (LOD), and label-free application (Honikel et al., 2018; Randviir and Banks, 2013).

3. Sensor surface material modifications

Material selection for biosensors is important for both improved sensitivity and selectivity, along with more stable bioreceptor immobilization and enhanced molecular recognition elements (MREs). Electrochemical biosensors need fast electron transfer between the active site of an MRE and the electrochemical transducer, which can be accomplished through different material combinations (Tertis et al., 2013). Advancements in material technology for biosensing have increased the popularity of carbon-based nanomaterials, such as fullerenes and nanotubes, due to their good electrical conductivity and their

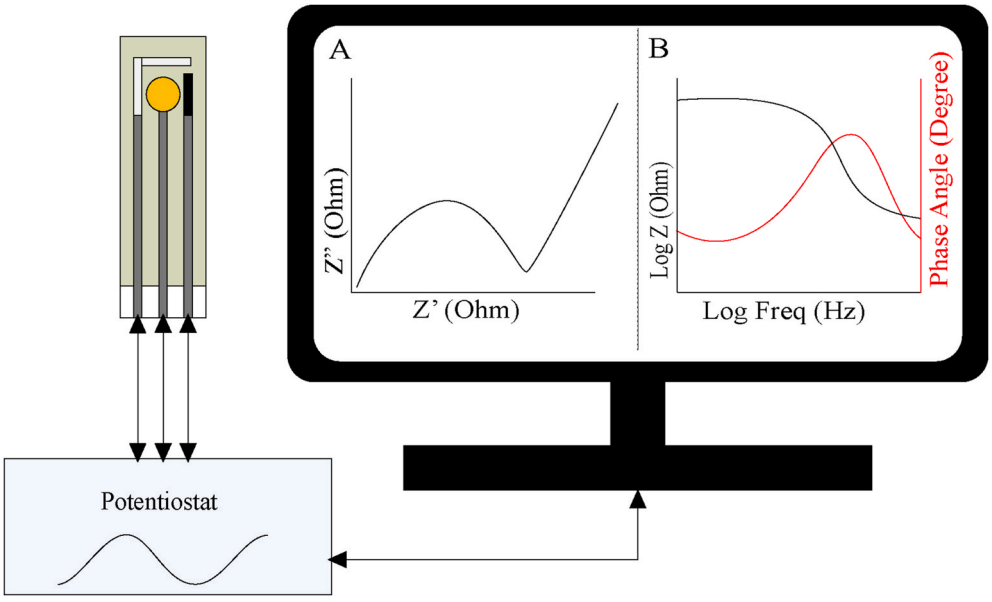

Fig. 2. Overview of EIS setup.

ability to form charge transfer complexes when in contact with an electron donor group (Barnes et al., 2007). Other materials that have made recent advancements are quantum dots, MXenes, conductive polymers, MoS_2 nanosheets, nanoparticles, metal-organic frameworks (Shi et al., 2017), and covalent organic frameworks (Wang et al., 2019).

Carbon nanotubes (CNTs) are hollow, single- or multi-walled, cylindrical nanotubes composed of rolled up graphene sheets. CNTs are being investigated for the improvement of transducers due to their large surface area, high electrical conductivity, unique tubular structure, good biocompatibility, and modifiable sidewall. The intention is to improve transducer analytical performance, automation, and miniaturization. Peptide modified multi-walled CNTs immobilized on a gold electrode have been used to detect low concentrations (10^2 CFU/mL) of *Escherichia coli* and *Klebsiella pneumonia* (Laurentius et al., 2016) and different oxidases can be applied for the detection of glucose, peroxides, L-lactate, acetaminophen, etc (Sandulescu et al., 2015).

Graphene is a one-atom thick sheet of sp^2 hybridized carbon, has a surface area twice as large as single-walled CNTs, and is a promising material for advancing analytical chemistry. Graphene's advantages include high mechanical strength, elasticity, and thermal conductivity, though it has poor dispersion in an aqueous medium (Sandulescu et al., 2015). Graphene can also be functionalized to advance aptasensor development by absorbing unfolded aptamer through π-π stacking interactions (Park et al., 2014). An aptasensor was recently developed to detect *Salmonella* using a graphene oxide chitosan complex, demonstrating an LOD of 10^1 CFU/mL (Dinshaw et al., 2017). Graphene has also been a key combination material with others such as conductive polymers. For example, the PPR3A composite, derived from the *BRCA1* tumor suppressor signal sequence and PR3A polymer, was synthesized on an electronically reduced graphene layer on a glassy carbon electrode (GCE) to detect *BRCA1* (Shahrokhian and Salimian, 2018).

Nanoparticles normally fall into one of five categories: magnetic, metal, semiconductor, polymeric, and hybrid nanoparticles. The most important types for electrochemical sensing are metal and hybrid nanoparticles (gold, silver, platinum, palladium, etc.), which have been used to immobilize biomolecules for sensing. Gold nanoparticles are the most commonly used due to their ability to form strong covalent bonds with thiol groups, while platinum and palladium have been used with single-and multi-walled CNTs to increase electrocatalytic activity along with improved conductivity (Sandulescu et al., 2015).

Other types of materials used in the biosensing field include nanostructured polymers (NPs) and molecularly imprinted polymers (MIPs). NPs are micropatterned surfaces serving as platforms for immobilization in electrochemical biosensing (Santos et al., 2010). MIPs are artificial macromolecular structures with properties mimicking biochemical processes, like receptor-ligand, antibody-antigen, and enzyme-substrate biorecognition (Sharma et al., 2012). The main advantages of MIPs compared to their biological counterparts include low cost, ease of preparation, long term stability and shelf life, reusability, high mechanical strength, and high chemical/thermal stability. To address MIP disadvantages such as lack of conductivity and electrocatalytic activity, MIPs have been combined with CNTs, graphene oxides, carbon dots, etc.

Quantum dots (QDs) are classified as manufactured semiconductor nanomaterials and have been identified as good candidates for biosensing applications due to their high luminescence, narrow emission, and low toxicity (Cotta, 2020). These properties are a result of their ability to produce bright colors when excited by light or electrical energy, and their size directly relates to how they absorb or emit energy. Recently, SiO_2@polydopamine core shell nanoparticles were used as a quencher for CdTe QDs to produce a photoelectrochemical immunosensor to detect an ovarian cancer marker, *CA125*, with high sensitivity (Xue et al., 2019). Graphene has also been used to modify the properties of QDs, and the zero bandgap exemplified from graphene quantum dots (GQD) prevents the emission of light when excited. GQDs have great promise in electrochemical biosensing as electrode modifiers due to their high speed electron transport, conductivity, and biocompatibility (Campuzano et al., 2019). Two-dimensional layered transition metal dichalcogenide nanosheets have recently gained attention in the field of biosensing due to their enhanced optical and electronic properties. Specifically, ultrathin MoS_2 nanosheets were compared to semiconductive MoS_2 nanosheets and demonstrate promise as candidates for rapid and sensitive fluorescence based biosensors for multiplexed DNA detection due to their heightened conductivity (Lan et al., 2018). While the properties of the above materials have previously been applied in optical sensing, they could hold promise in the realm of electrochemical sensing when used in combination with other modifications (Campuzano et al., 2019).

Recently developed MXenes are 2D multi-layered nanomaterials made of a transition metal and a carbon or nitrogen. They have been especially attractive as a new design component for electrochemical biosensors due to their ability to provide an efficient immobilization medium. (Khan and Andreescu, 2020). MXenes are a promising material, characterized through impedimetric methods, for the continuous, enzymatic, amperometric detection of biomarkers involved in renal function such as uric acid, creatinine, and urea (Liu et al., 2019). EIS characterization showed that MXenes performed better in electron transfer, catalytic activity, absorption capabilities, and had a lower interfacial resistance compared to graphene, indicating its potential use for impedimetric detection.

4. Single marker EIS biosensing

Recent advances using EIS techniques in biosensing applications vary significantly by target analyte type and bioreceptor used. The selection of the molecular recognition element (MRE) is dependent upon the characteristics of both the analyte and transducer type of the sensor. Common bioreceptors previously used in EIS sensors include enzymes, antibodies, artificial binding proteins, aptamers, and bacteriophages. Each type of MRE has its own advantages and disadvantages in terms of selectivity, specificity, and detection time. Fig. 3 portrays the possible applications of EIS broken up by MRE type.

4.1. Enzymes

Enzymes are one of the most frequently used MREs due to their high specificity, high binding affinity, and catalytic characteristics. The mechanism for enzymatic sensing involves a catalytic reaction where a biochemical product is formed, which is then measured through various physicochemical properties. Immobilized enzymes are relatively stable compared to mobile enzymes, while also having the capability of continual and repetitive use (Nguyen and Kim, 2017). Impedimetric-based enzymatic biosensors are not as common as amperometric or potentiometric sensors but have recently shown promise in sensing a variety of analytes, such as glucose, glutamate, urea, and diazinon.

The development of enzyme sensors for glucose detection involves three types according to the electron acceptor: first, second, and third generation. In first generation sensors, oxygen acts as the electron acceptor, thus producing hydrogen peroxide. The detection of decreasing oxygen or increasing hydrogen peroxide is therefore an indication of electron transfer produced from the enzymatic reaction between the oxidase enzyme and glucose (Ferri et al., 2011). Second generation sensors employ artificial mediators, or redox dyes, as the electron acceptors. The electrochemical measurement of the reduced mediators thus indicates enzymatic activity without interference of other redox species. Third generation sensors use direct electron transfer (DET)-type enzymes with the ability to transfer electrons without artificial mediators or oxygen.

First generation glucose sensors are common for monitoring the glycemic profile of diabetic patients. To further improve measuring the glycemic severity and variability, Adamson et al. (2014) developed an enzyme-based EIS sensor to detect 1,5-anhydroglucitol (1,5-AG) levels,

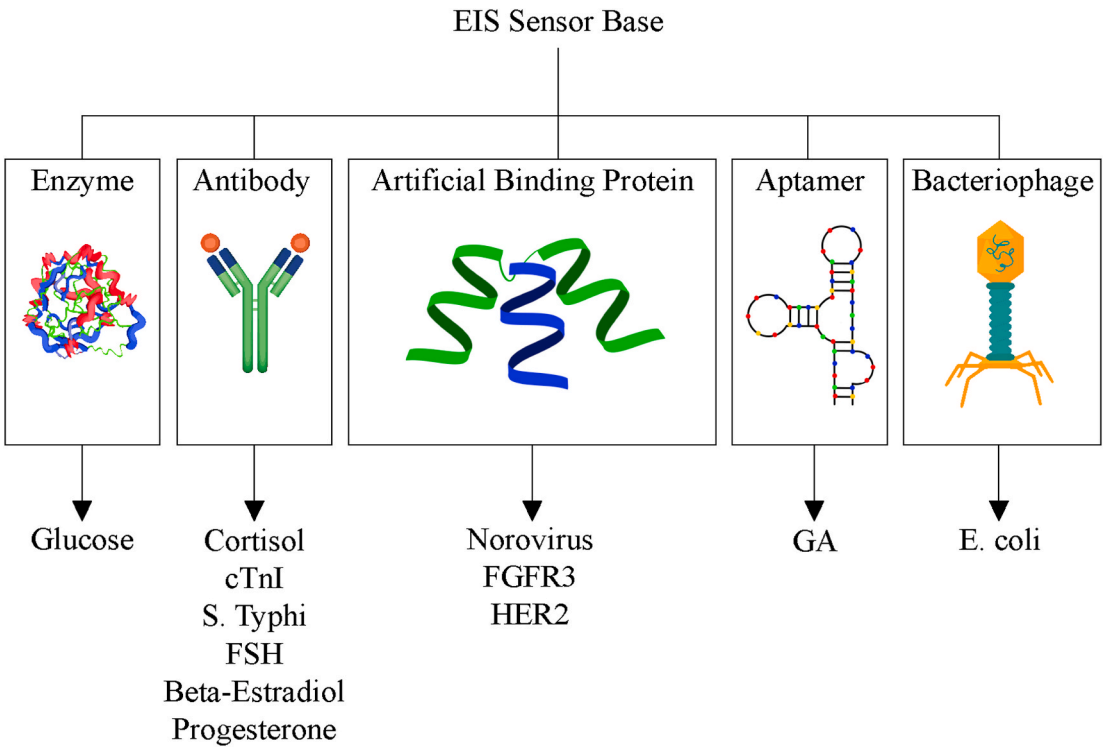

Fig. 3. Representation of different analyte detection based on bioreceptors.

another biomarker of the glycemic profile. The enzyme pyranose oxidase (POx) was used in conjunction with a solution containing its cofactor, flavin adenine dinucleotide (FAD), and ferricyanide to oxidize 1,5-AG into hydrogen peroxide. POx was immobilized on a self-assembling monolayer (SAM)-modified gold electrode. EIS was performed to detect purified 1,5-AG over a range of 0–300 mg/dL, and the OBF was determined to be 3.71 Hz. The response of a single electrode at a lower concentration range (0.8–12 mg/dL) was measured at 3.71 Hz. In combination with the higher concentration range (10–300 mg/dL) taken over six electrodes, the average R^2 and slope were 0.96 and 7.04 Ω/(log(mg/dL)), respectively. The relative standard deviation (RSD) was reasonably high (26–28%) for the higher concentration range, and subsequent experiments confirmed that 1,5-AG detection was only desirable in low blood concentrations. The proposed faradaic EIS sensor for 1,5-AG would be most beneficial in samples of normal to hypoglycemic ranges, and further optimization and manufacturing are required (Adamson et al., 2014).

More recently, a third generation DET-type enzyme sensor was developed using faradaic EIS principles to detect glucose concentrations on a gold disk electrode (GDE). A FAD-dependent glucose dehydrogenase (GDH) complex was employed, using FAD as a primary electron acceptor for the catalysis of the first hydroxyl group on glucose. The faradaic impedance of the DET-type FADGDH complex was compared to a mutated, non DET-type complex using EIS in the presence of different glucose concentrations without a redox probe. EIS was performed over a frequency range of 100 kHz to 5 mHz, at an amplitude of 10 mV, and superimposed over +100 mV DC vs. Ag/AgCl. The DET-type FADGDH modified GDEs resulted in decreased R_{ct} values with increasing glucose concentrations between 1 and 100 mM. The non-DET-type complex resulted in no impedance change in response to increased glucose concentrations, indicating the need for redox probes to perform electron transfer for non-DET-type enzymes. Further experimentation confirmed that both DC bias and length of the self-assembling monolayer (SAM) affect $\Delta(1/R_{ct})$ values. Impedance measurements at a fixed frequency of 5 Hz over a glucose range of 0.02–0.2 mM produced a calibration curve with an R^2 value of 0.996 and a slope of 3.1×10^7 mM. Additionally, the glucose dependency of imaginary impedance is observable at frequencies lower than 15 mHz compared to observable frequencies lower than 2.5 mHz for real impedance. The work presented a highly sensitive, third generation, enzyme-based faradaic EIS sensor without the use of a redox probe for glucose detection (Ito et al., 2019).

4.2. Antibodies

Immunosensors describe a broad category of antibody-based sensors that generally provide high specificity for their antigen. Types of antibodies applied to immunosensors include monoclonal, polyclonal, recombinant, fragments (Fb/Fb'), and recombinant fragments (Fv).

One of the most researched target analytes for detection using EIS-based immunosensors is cortisol, a hormone released during stress. A label-free, paper-based POC immunosensor was developed to measure cortisol concentrations in saliva samples while eliminating the need for a redox probe and reducing production cost. Monoclonal cortisol antibodies were conjugated on SAM-modified gold microelectrodes arranged into square rings to improve sensitivity and dynamic sensing. The gold electrodes were deposited on a graphene-polymer composite that was spin-coated onto filter paper. The biosensor was integrated with a printed circuit board to wirelessly send signals using MATLAB. The sensor provided sensitive results comparable to an ELISA (1.5–3.7% variation), with a detection range of 3 pg/mL to 10 μg/mL, detection limit of 3 pg/mL, and R^2 of 0.9951 (Pan et al., 2017). The design of this cortisol immunosensor showed promise in providing a cost-efficient, highly sensitive, and fast response for on-site diagnostics and commercialization.

A microfluidic chip was developed by Singh et al. (2017) to measure levels of cardiac troponin (cTnI). A manganese-reduced graphene oxide nanocomposite was constructed in a flower-shaped structure to increase the number of cTnI monoclonal antibodies bound to the surface. EIS was performed over an incubation time of 3 min to measure antibody-antigen binding through the microfluidic device. Experimentation with a cTnI concentration range of 0.008–20 ng/mL resulted in a detection range of 0.8–20 ng/mL, detection limit of 0.03 ng/mL,

response time of 100 s, R^2 of 0.992, and shelf life of 30 days at 4 °C. Increasing concentrations yielded a linear increase in R_{ct}, which could be a response to an inhibited electron generation from redox conversion. The biosensor also showed relatively high selectivity for cTnI when tested with four interferents (myoglobin, cTnC, cTnT, and B-type natriuretic peptide) (Singh et al., 2017). The fabrication of the manganese-reduced graphene oxide nanocomposite in its flower formation provided a highly sensitive device for monitoring relatively low concentrations of cTnI.

The stability of immobilized whole antibodies on sensor surfaces is difficult to achieve with passive binding, which also causes random orientations. However, surface modifications, such as SAMs, allow directed antibody orientation to expose the antigen-binding regions while maintaining the antibody's native conformation. Other surface modification techniques to improve sensitivity and uniform coverage involve receptor binding to the Fc segment of the antibody or immobilizing antibody fragments through sulfhydryl groups. To overcome multi-step immobilization and functionalization, the antibody itself can be chemically modified for enhanced stability, orientation, and binding onto the sensor surface. More specifically, sulfur-derived chemical modifications of covalently-coupled antibodies can provide a site-directed, self-assembly of antibodies onto a gold surface (Acero Sánchez et al., 2016).

Advancements in single marker, impedance-based immunodetection of pathogens have been made to detect the presence and concentration of harmful microorganisms. *S. Typhimurium* was detected on a gold interdigitated array microelectrode (IDAM) which was immobilized with streptavidin and biotin-labelled *S. Typhimurium* antibody. Impedance measurements were recorded at a frequency range of 1 Hz to 1 MHz for a concentration range of 76–7.6 × 10^6 CFU/50 μL. The most significant impedance change between the bacteria and control sample (a 35% increase) was at 101 Hz, resulting in a correlation coefficient of 0.98. The immunosensor demonstrated high specificity and low detection time of 1 h compared to traditional methods, confirming the viability of a low-cost, portable rapid detection system for *S. Typhimurium* (Wen et al., 2017).

The specificity of antibody binding was demonstrated by separately quantifying three fertility hormones, β-estradiol, progesterone, and follicle stimulating hormone (FSH), using EIS technology. The sensor consisted of a GDE working, an Ag/AgCl reference, and a Pt counter electrode. A 16-MHDA SAM layer was bound to the GDE, and through activation using EDC/NHS solution, the respective antibodies were immobilized. The impedance change over increasing analyte concentrations was measured over a frequency range of 0.1 Hz–100 kHz and fixed formal potential of 150 mV. The imaginary impedance increased with increasing FSH, estradiol, and progesterone concentrations (1–500 pg/mL, 0.1 to 10,000 pg/mL, and 0.01–100 ng/mL, respectively). From these overlays, the OBFs for FSH, estradiol, and progesterone were determined to be 175.8, 8.071, and 1.74 Hz, respectively. At these OBFs, calibration curves generated LODs and R^2 values of 4.02 pg/mL and 0.91 for FSH, 2.35 pg/mL and 0.8 for estradiol, and 8.22 ng/mL and 0.86 for progesterone. The differences in OBF indicate the possibility for an efficient multimarker device to detect all three analytes. Nontarget testing was conducted using the anti–FSH–immobilized GDE and varying concentrations of progesterone, albumin, and estradiol. The strong response to FSH in comparison to the other three molecules confirms the high selectivity of the sensing platform. Detection capabilities of the sensor platform in whole blood was then analyzed using 1–90% whole blood samples. The anti-FSH testing indicated significant interference, whereas the anti-estradiol demonstrated little interference, signifying a need for a filtration method. Thus, the proposed sensor system for individually testing three target analytes shows promise for future work in multimarker detection using antibodies (Khanwalker et al., 2019).

4.3. Artificial binding proteins and peptides

Synthetic binding proteins and peptides are engineered proteins designed to bind to a specific molecule. Affibody molecules are a general class of artificial binding proteins and include affimers, monobodies, anticalins, DARPins, etc. They are polypeptides in structure and consist of natural amino acids constructed using non-antibody/molecular scaffolds (Sha et al., 2017). An advantage of artificial binding proteins pertaining to their molecular recognition is their ability to be chemically synthesized, which allows for a vast amount of flexibility in target modifications (Bazin et al., 2017). Their small molecular weight makes artificial binding proteins more stable in a large range of buffer solutions. Alternative scaffold proteins were designed to address the limitations of antibodies by combining more favorable molecular recognition properties of antibodies with smaller molecular weight, higher stability, and more options for multi-specific recognition systems. They also have the advantage of lowered production costs and little to no batch-to-batch variation (Thangsunan et al., 2021). There have been many advancements made in the area of artificial binding proteins and peptides with regards to molecular markers for biosensing. Many have produced high target molecule sensitivity with significantly lower LOD compared to other diagnostic counterparts.

Affibodies have a triple α helical bundle structure and are able to demonstrate binding specificity to many different types of proteins such as: insulin, fibrinogen, transferrin, tumor necrosis factor–α, etc (Bazin et al., 2017). Affibody's high selectivity and high binding affinity is essential to *in vitro* and *in vivo* diagnostics. They have been the most promising candidates for tracing human epidermal growth factor receptor type–2 (HER2) compared to antibodies, antibody fragments, and designed ankyrin repeat proteins (Löfblom et al., 2010). Anticalins have a β-barrel architecture with an attached α helix and are chosen for their natural ability to bind to small molecules using their barrels and loops (Sha et al., 2017). This synthetic protein scaffold is most commonly used for *in vivo* molecular positron emission tomography imaging due to its good tumor uptake, retention, and contrast (Stern et al., 2013). DARPins, designed ankyrin repeat proteins, are approximately 20 kDa and have an extended binding surface due to their repetitive structural units. This artificial binding protein system has the capacity to form a good foundation for biosensing platforms including the giant magnetoresistance biosensor for recognition of the ESAT-6 protein for early tuberculosis detection (Gupta and Kakkar, 2019).

Recently a label free detection of human norovirus was demonstrated using the Noro-1 and Noro-2 peptides. The LOD of Noro-1 peptide (1.44 μg/mL) was approximately twice as sensitive compared to Noro-2 peptide (3.96 μg/mL). Peptides were created using evolutionary phage display and analyzed via faradaic EIS. The electrode platform consisted of a gold working, a palladium counter, and Ag/AgCl reference electrode. The Noro-1 peptide based biosensor exhibited high affinity for its norovirus target and is exemplified by its LOD (>10^2 norovirus particles) compared to traditional forms of norovirus detection. These include the rapid immunochromatographic kit (3.2 × 10^6), IDEIA norovirus kits (1.6 × 10^7), and reverse transcription-PCR combined with fluorescence microscopy (6 × 10^7) (Hwang et al., 2017).

An affimer-based sensor has also been developed to detect the fibroblast growth factor receptor 3 (FGFR3), which is commonly overexpressed in bladder cancers. This biosensor offers the possibility of a noninvasive option for diagnosing bladder cancers, compared to the traditional immunohistological staining of biopsied patient tumors. A Dropsens sensing platform consisting of a gold working, gold counter, and silver/silver chloride electrode was used for affimer immobilization and EIS analysis. Of the three randomly selected affimers, anti-FGFR3-14 and anti-FGFR3-21 showed the highest binding affinity to FGFR3 at an optimal immobilized concentration of 1 μM. The linear range of detection for FGFR3-14 and FGFR3-21 was found to be 0.01 pM to 0.1 nM at an R^2 of 0.9553 and 0.8813 for the percent change in R_{ct}, respectively. These results represent the impedimetric response of

FGFR3 binding in a 10 mM ferri/ferrocyanide redox medium. Synthetic urine samples of three volumetric concentrations were spiked with FGFR3 and EIS was run with a bovine serum albumin (BSA) antifouling agent applied to the surface of the Dropsens electrodes. It was found that anti FGFR3-21 affimer sensors with 10% (v/v) synthetic urine spiked with FGFR3 showed the best response. The determined linear range of detection was 0.1 pM to 0.1 nM with an R^2 of 0.9428 (Thangsunan et al., 2021).

There have also been significant strides made in the detection of biomarkers for breast cancer, specifically human epidermal growth factor 2 (HER2). A label-free affisensor was developed to detect the presence of *HER2* proto oncogene in human serum samples. Graphene screen printed electrodes with a gold working, gold counter, and Ag/AgCl reference electrode were used. Anti-HER2 affibodies were immobilized using 0.1 mM 6-mercaptohexanol (MCH) as its SAM on screen printed electrodes. Electrochemical measurements identified an OBF of 115 Hz for HER2 immersed in a 0.01 M ferricyanide redox probe. The affibody-HER2 calibration curve representing the change in R_{ct} produced an R^2 of 0.98 with an LOD of 6 μg/L in the range of 0–40 μg/L. The same trends were present when serum samples spiked with HER2 were used (Ravalli et al., 2015).

4.4. Aptamers

Artificial aptamers are similar to antibodies because they provide a high binding affinity for their target analyte, but differ due to their composition of nucleic acids, such as DNA or RNA oligonucleotides. Aptamers maintain their stability in a range of environments and are relatively small and flexible, providing the ability to target small or otherwise inaccessible molecules (Zhou and Rossi, 2017). The aptamer production process allows for chemical modifications to tailor the aptamer for the target of choice, making this group of recognition elements desirable for highly selective biosensing. There is a wider range of target analytes for aptamers compared to other MREs, including viruses, nucleic acids, proteins, peptides, cells, and small organics (McKeague and Derosa, 2012). During electrochemical detection, the system can either be in *signal on* or *signal off*; both use a redox label to detect a target binding with the aptamer. During this process, a conformational change in the aptamer is produced, moving the redox label either closer to the electrode or further away, producing a measurable signal. The system can also be label-free, involving the addition of a redox molecule to the aptamer, which then gets released once the target binds to the aptamer (Hong and Sooter, 2015).

Monitoring glycated albumin (GA) is utilized to detect changes in glycemic conditions for patients under diabetes treatment. Albumin, a high molecular weight protein (66 kDa), was analyzed by Farzadfard et al. (2020) for an electrochemical based aptasensor measuring GA. The setup in this study consisted of an IviumStat electrochemical station, glassy carbon working electrode, and a three-electrode cell. The immobilization protocol consisted of mixing graphene-gold nanoparticles with thiolated anti-GA aptamer. Prior to application, the gold-aptamer was mixed with a 1% Nafion solution in a 4:1 ratio. The final solution was then placed on the electrode and tested with EIS. Conducting EIS on the aptasensors revealed GA binding on the electrode surface, demonstrated through an increase in charge transfer resistance of the ferrous/ferric reaction. The LOD was determined to be 0.09 mg/mL using potassium ferrocyanide. Potassium ferrocyanide was then replaced with methylene blue (MB) because cyanide has a hazardous nature and does not allow the labeling of the aptasensor in a buffered media. With the modified electrode in the MB solution, a LOD of 0.07 μg/mL was obtained through a range of 2–10 μg/mL. The fabricated biosensor demonstrated the desired performance for detecting GA macromolecules and evaluating hyperglycemic conditions (Farzadfard et al., 2020).

4.5. Bacteriophages

Bacteriophages are viral agents which are relatively stable under extreme conditions, such as ranges of pH and temperatures. The main application of bacteriophages is for bacterial detection through infecting and replicating within bacteria. This also allows them to differentiate between live and dead bacteria, making them a preferred MRE over enzymes (Ahmed et al., 2014). Combined with EIS, bacteriophages provide a highly specific, stable, and cost-effective diagnostic utility for bacteria in which low concentrations can be recognized. Rapid detection of bacterial species can be accomplished by monitoring the electrochemical properties of the bacteriophage and bacteria binding event (Bhardwaj et al., 2016).

The nondestructive nature of EIS delivers a safe detection technique for microbial analysis, as explored by a non-lytic M13 phage-modified electrochemical biosensor for *E. coli*. AuNPs were electrodeposited onto a polished glassy carbon electrode (GCE) to increase the surface area and amplify electron transfer. A 3-mercaptopropionic acid (MPA) SAM was applied and the sensors were incubated in an M13 phage solution, acting as the MRE. The functionalized sensor was immersed in bacterial cell suspension for 30 min, which was previously found to be the optimal incubation time. EIS was performed in potassium ferricyanide redox solution at the formal potential of 0.15 V, derived from cyclic voltammetry (CV) tests, and a frequency range of 1–10^4 Hz. The results demonstrated an R_{ct} increase in response to increased *E. coli XL1-Blue* concentrations (10–10^7 CFU/mL). The R_{ct} response correlated linearly with the log of bacterial concentration between 10 and 10^5 CFU/mL, with a sensitivity of 7.78 Ω/log (CFU/mL)) and LOD of 14 CFU/mL. The biosensors demonstrated high reproducibility with a standard deviation of 1.12–2.57 and RSD of 4.46–8.47%. Comparison of the functionalized sensor to an unmodified Au-GCE confirmed an efficient biofunctionalization protocol by providing minimal response in the control sample. Further, the cytosensor selectivity was analyzed by comparing *E. coli KL1-Blue* and *K12* with *P. chlororaphis*, resulting in similar responses with both *E. coli* samples and minimal response with *P. chlororaphis*. The cytosensor demonstrated high stability over 16 days, temperatures up to 45 °C, and in a pH range between 3 and 10. The proposed cytosensor exhibits the wide range of advantages in using bacteriophages as the MRE for bacterial detection (Sedki et al., 2020).

Table 1: Comparison of different analytes detected using EIS techniques. Abbreviations include: 1,5-anhydrogluticol (1,5-AG), Norepinephrine (NE), B type natriuretic peptide (BNP), C reactive protein (CRP), Cardiac troponin I (cTnI), Follicle stimulating hormone (FSH), Glial fibrillary acidic protein (GFAP), Interferon gamma (IFN-γ), Interleukin-10 (IL-10), Interleukin-2 (IL-2), Neutrophil gelatinase-associated lipocalin (NGAL), Progesterone (P4), Tumor specific necrosis factor α (TNF-α), Interluekin-12 (IL-12), *S. typhimurium* (*S.typhi*), *Escherichia coli* (*E. coli*), Neuron-specific enolase (NSE), Norovirus (Noro), Fibroblast growth factor receptor 3 (FGFR3), Human epidermal growth factor 2 (HER2), Glycated albumin (GA).

5. Multimarker EIS diagnostics

Recently, EIS has shown significant promise in the ability to sense multiple biomarkers on one sensor, also known as multimarker detection. This method of detection can be done several different ways, but OBFs show promise in allowing multiple MREs to be attached to a single transducer, potentially allowing smaller diagnostic devices with high specificity, responsivity, and rapid assessment (Cardinell et al., 2019a). The OBF is specific to individual biomarkers, making simultaneous detection possible. Multiplex systems are applicable in a variety of industries, such as monitoring multiple biomarkers in a diabetic patient's glycemic profile to enable a complete and informed diagnostic tool (Lin et al., 2017). Two techniques can be implemented to achieve multiplexed detection. The first is using multiple transducers with different MREs, whereas the second technique is distributing different MREs on

Table 1
Summarizes the discussed single marker EIS applications, sorted by MRE.

Analyte	MRE	Physiological Range	Detection Range	LOD	Reference(s)
1,5 - AG	Enzyme	0.1–12 mg/dL	0–300 mg/dL	27.29 mg/dL	Adamson et al. (2014)
Glucose	Enzyme	1.25–50 mM	0–100 mM	–	Ito et al. (2019)
NE	Enzyme	70–1700 pg/mL	0–10000 pg/mL	98 pg/mL	Haselwood and la Belle (2015)
BNP	Antibody	0.1–100 pg/mL	0–10000 pg/mL	100 pg/mL	Deng et al. (2019)
β-estradiol	Antibody	10–500 pg/mL	1–500 pg/mL	2.35 pg/mL	Khanwalker et al. (2019)
CRP	Antibody	0.3–10 μg/mL	0–10 μg/mL	3 mg/L	Deng et al. (2019)
cTnI	Antibody	0.006–50 ng/mL	$1e^{-5}$-300 ng/mL	–	Deng et al. (2019); Mahajan and Jarolim (2011)
cTnI	Antibody	0.006–50 ng/mL	0.8–20 ng/mL	0.03 ng/mL	Singh et al. (2017)
Cortisol	Antibody	82.8–552 nM	138 pM-552 nM	59.76 nM	Cardinell et al. (2019b)
Cortisol	Antibody	82.8–552 nM	3 pg/mL-10 μg/mL	3 pg/mL	Pan et al. (2017)
FSH	Antibody	0.1–10000 pg/mL	0.1–10000 pg/mL	4.02 pg/mL	Khanwalker et al. (2019)
GFAP	Antibody	46–1386 pg/mL	0.1–2800 pg/mL	2.3 pg/mL	(Cardinell et al., 2019a; Jany et al., 2015)
Insulin	Antibody	100–2000 pM	50–1500 pM	14.46 pM	Malkoc et al. (2017)
IFN-γ	Antibody	0.1–100 pg/mL	0–10000 pg/mL	–	Fairchild et al. (2009); Hussain et al. (n.d.)
IL-10	Antibody	4.8- >10 pg/mL	0–10000 pg/mL	–	Fairchild et al. (2009); Sarris et al. (1999)
IL-2	Antibody	241–846 U/mL	0–10000 pg/mL	–	Fairchild et al. (2009); Hayden et al. (2017)
NGAL	Antibody	37–922 ng/mL	0–1000 ng/mL	101.9 ng/mL	Gonzalez and la Belle (2012)
P4	Antibody	0.1–100 ng/mL	0.1–100 ng/mL	8.22 ng/mL	Khanwalker et al. (2019)
TNF-α	Antibody	0.1–75 pg/mL	0.1–75 pg/mL	0.55 pg/mL	Cardinell et al. (2019a)
IL-12	Antibody	0–18.6 pg/mL	0.1–100 pg/mL	3.5 pg/mL	Bhavsar et al. (2009)
S. typhi	Antibody	50–1300 CFU/mL	76–7.6 × 10^6 CFU/50 μL	7.6 × 10^2 CFU/50 μL	Killar et al. (1986); Wen et al. (2017)
E. coli O157:H7	Antibody	50–1x10^9 CFU	0–1x10^5 CFU/mL	100 CFU/mL	Wan et al. (2016); Cai et al. (2015)
NSE	Antibody	0.1–16.6 ng/mL	0–25 ng/mL	28.02 pg/mL	Honikel et al. (2019)
Noro-1	Peptide	–	0.01–1000 μg/mL	1.44 μg/mL	Hwang et al. (2017)
Noro-2	Peptide	–	0.01–1000 μg/mL	3.94 μg/mL	Hwang et al. (2017)
FGFR3	Affimer	–	0.01 pM - 0.1 nM	18.5 pM	Thangsunan et al. (2021)
HER2	Affimer	–	0-40 μg/L	6 μg/L	Ravalli et al. (2015)
Glycan-lectin	Lectin	0–100 ng/mL	0–100 ng/mL	–	la Belle et al. (2007)
GA	Aptamer	6–30%	2–10 μg/mL	0.07 μg/mL	Farzadfard et al. (2020)
E.coli XLI-Blue	Bacteriophage	–	10–10^5 CFU/mL	14 CFU/mL	Sedki et al. (2020)

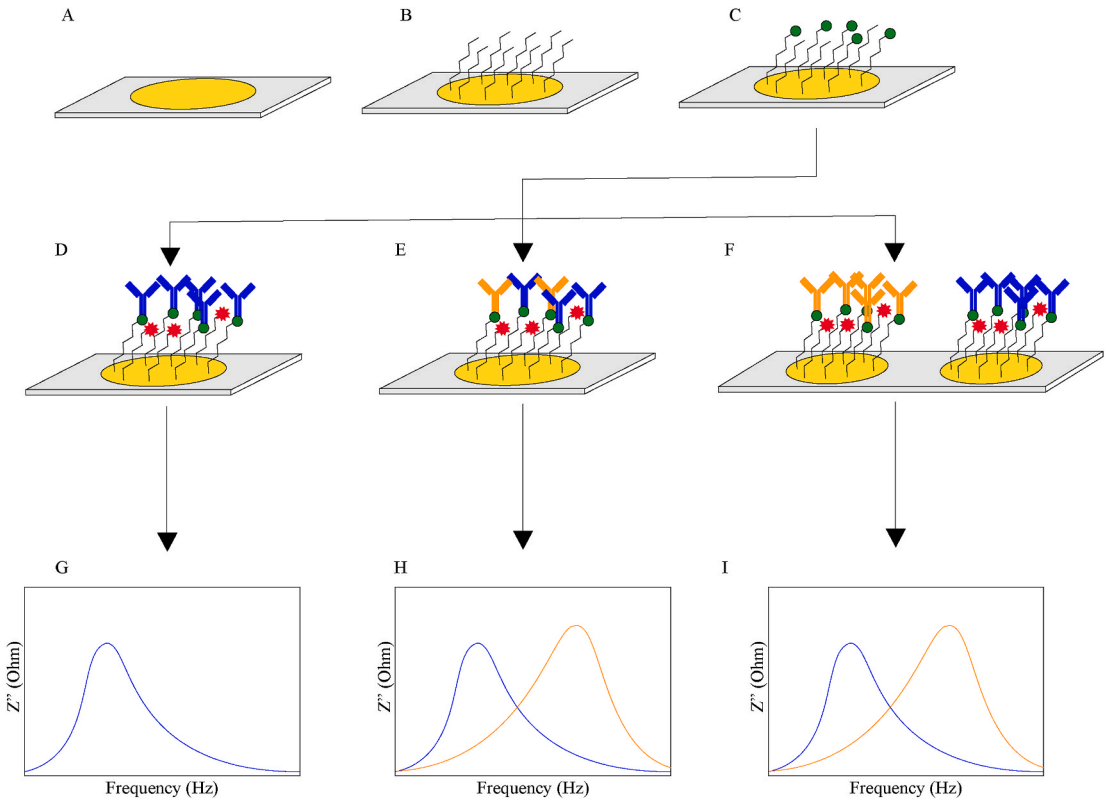

Fig. 4. Diagram of a single marker versus multimarker immobilization approaches. (A) Represents a bare gold surface, (B) addition of SAM layer, (C) modification using EDC/NHS (green dots), (D) single MRE immobilization (blue molecule) with blocking layer (red dots), (E) multimarker MRE immobilization (blue and orange molecules) with blocking layer on one electrode, and (F) multimarker MRE immobilization with blocking layer on multiple electrodes. When the resulting signals are obtained, (G) shows the signal from one marker, (H) shows the signal from multiple markers which will need to be decoupled, and (I) shows the signal from multiple markers overlayed with each other. These signals can be used to determine the OBFs of the different markers. (For interpretation of the references to color in this figure legend, the reader is referred to the Web version of this article.)

single or multiple electrodes. Multimarker detection can also be obtained in both faradaic and non-faradaic applications, depending on the diagnostic setting. Fig. 4 shows a high-level comparison of single versus multimarker immobilization procedure on a GDE platform, based on the work of Cardinell et al. (2019a), Lin et al. (2017), and Honikel et al. (2019).

The method of placing two MREs on two sensors and a single substrate was utilized to develop a dual-marker, non-Faradaic, POC biosensor for C-Reactive protein (CRP) and Procalcitonin (PCT), two biomarkers of sepsis. PCT is a protein which is negligible in a healthy system, whereas the concentration can increase up to 5000-fold within 2–8 h of infection. CRP is another protein which increases up to 1000-fold upon inflammation and infection, beginning as early as 12 h upon infection and lasting up to 7 days. Fabrication was accomplished by placing gold interdigitated electrodes on a polyimide substrate, followed by a thin layer of ZnO, and separation of two sensors using an encapsulant. A thiol-based cross-linker was added to the surface, which allowed immobilization of PCT antibody on one sensor and CRP antibody on the other, followed by a blocking agent. A control was produced with blank buffer (serum and whole blood), and sequential concentrations of PCT and CRP in spiked serum and whole blood were separately added and measured. PCT was tested from a range of 0.01–10 ng/mL in both serum and whole blood, resulting in an R^2 of 0.99 and 0.98, respectively. The range for CRP was 0.01–20 μg/mL in serum and 0.01–10 μg/mL in whole blood, resulting in an R^2 of 0.90 and 0.98, respectively. There was a decrease in impedance and increase in capacitance as both the PCT and CRP concentrations increased, with the OBF determined to be 10 Hz for PCT and 100 Hz for CRP. The LOD was found to be 0.10 ng/mL for PCT in both solutions and 0.10 μg/mL for CRP in both solutions. The selectivity and specificity of the biosensor was examined under a solution of BSA, which resulted in a significantly smaller change in response compared to PCT and CRP solutions. This work overcomes the challenges in current clinical methods for these markers, such as low specificity, low sensitivity, large sample volume, and delayed results (Tanak et al., 2019).

Work by Cardinell et al. (2019a) aimed to increase the diagnostic methods available for validating traumatic brain injury (TBI). Common biomarkers of TBI include neuron specific enolase (NSE) and S100 calcium-binding protein β (S-100β). Both biomarkers were characterized individually, along with the additional TBI markers, glial fibrillary acidic protein (GFAP) and tumor necrosis factor-α (TNF-α), using a multistep immobilization process on GDEs. 16-MHDA was immobilized on the GDE platform, followed by chemical modification of the SAM through EDC/NHS. The respective antibody(ies) were then incubated on the surface, followed by an ethanolamine treatment. Each TBI marker was validated in purified, spiked blood, and plasma samples. The multimarker NSE and S-100β sensor was tested in injured rat controlled cortical impact (CCI) plasma samples over 14 days with faradaic EIS. Purified samples were tested over the following ranges: NSE (1–25 × 10^3 pg/mL), S-100β (1–10 × 10^3 pg/mL), GFAP (0.1–2800 pg/mL), and TNF-α (0.1–75 pg/mL). Individual biomarkers yielded the following OBFs and optimal assay measurement times: NSE (546.9 Hz, 13 s), S-100β (2148 Hz, 15 s), GFAP (17.44 Hz, 3 s), and TNF-α (57.44 Hz, 2 s). Spiked plasma testing showed a high R^2 (0.94–0.97) at the 12.5% diluted plasma sample in PBS, which is what the rat CCI plasma samples were tested at. The rat study for the multimarker device was conducted using mild and moderate CCI rats, with NSE and S-100β being tested at their unique OBFs. Results showed a complex impedance range of 1.02–1.08 Ω for S-100β over the 14 days, which correlates to a ~840-776 pg/mL concentration range during the period. NSE showed a similar impedance range over the same period, 1.03–1.06 Ω, but correlated to a ~513–523 pg/mL range. S-100β readings were shown to be higher than NSE but both markers were shown to increase slightly over the first 3–7 days then experience a decrease, which aligns with other reported rat models in cerebrospinal fluid (Cardinell et al., 2019a).

Coronary vascular disease (CVD) is the leading cause of death of over 800,000 people in the United states per year. Key biomarkers for this disease include low density lipoproteins (LDL) and high density lipoproteins (HDL). Work by Lin et al. (2017) shows promise for developing a dual biomarker detection platform for these two proteins using a faradaic approach. To develop the detection platform, GDEs were immobilized with 16-MHDA, then treated with EDC/NHS, LDL and HDL antibodies at a 1:1 ratio, and ethanolamine, in that order. The developed sensor was characterized with the individual markers (LDL or HDL) over a 0–50 mg/dL range and both markers simultaneously (LDL and HDL) over a range of 0–10 mg/dL range using EIS. Purified samples on the individual markers yielded an OBF of 81.38 Hz ($R^2 = 0.92$) for LDL and 5.49 Hz ($R^2 = 0.97$) for HDL using an imaginary impedance analysis approach. In comparison to complex impedance, imaginary impedance theoretically allows optimal signal distinguishment through easier signal decoupling in a multimarker approach. This is due to distinct analyte peaks brought on by capacitive changes. These OBFs were shown to shift during the co-immobilization, with LDL changing to 175.8 Hz ($R^2 = 0.88$, Slope = 57.15 Ω/(mg/dL)) and HDL moving to 3.74 Hz ($R^2 = 0.99$, Slope = 199.4 Ω/(mg/dL)). Both of these markers exhibited high slopes and R^2 during the co-immobilization, allowing easier signal decoupling with the imaginary impedance approach. The LOD of the dual sensor was 1 mg/dL for each marker and the individual markers had a dynamic range of 35.78 mg/dL–211.22 mg/dL for LDL and 42.43 mg/dL–172.65 mg/dL for HDL. The author expands on the link between OBF and target analyze size, orientation, and dissociation rates, stating that the seen OBF shift could be attributed to interaction of these variables (Lin et al., 2017).

Recently, a three-dimensional paper-based electrochemical impedance device (3D-PEID) was developed by Boonyasit et al. (2015) for sensing total and glycated hemoglobin (HbA1c). HbA1c is used for monitoring long term glycemic control in diabetes patients. In the experiment conducted, the MREs used were haptoglobin (Hp) or 3-aminophenylboronic acid (APBA)-modified eggshell membranes (ESM). The ESM-impedance sensor was developed by immobilizing APBA or Hp on the surface through glutaraldehyde crosslinking. The multiplexing sensor developed consisted of a dual-screen printed electrode on wax patterned paper integrated with a magnetic paper multilayer. Total hemoglobin was tested from a range of 0.5–20 g/dL, producing an R^2 of 0.989. HbA1c was tested across a range of 2.3–14%, with an R^2 of 0.997 with a detection limit of 0.08 g/dL. The OBF for total hemoglobin was 5.18 Hz and 9.99 Hz for HbA1c. The developed 3D-PEID device can increase data acquisition time by a factor of 15 with a select frequency value when monitoring multiple diabetes markers with a single EIS platform. A clinical study was conducted to validate the capability of the 3D-PEID device. The study measured the analytical performance of the device using human serum albumin and non-glycated hemoglobin (HbAo) on the prepared Hp-modified ESM and APBA-modified ESM sensor. The evaluated concentration range was 3–6 g/dL for human serum and 10–20 g/dL for HbAo. The assessment concluded with a 95% confidence interval for the 3D-PEID technique and turbidimetric inhibition immunoassay, with a total hemoglobin range of 0.113–0.8916 g/dL and 0.9439–0.9929, respectively. HbA1c analysis covered a range of −0.0200–0.4453% and 0.9227 to 1.0000, respectively. Through this validation, the 3D-PEID device exemplified great sensitivity and a vast detection range for total hemoglobin and HbA1c values within accepted clinical ranges (Boonyasit et al., 2015).

A multiplexed detection system was previously developed for the simultaneous detection of two *E. coli* genes, *yaiO*, and its virulent variant, *f17*. The fabrication consisted of a screen printed carbon electrode (SPCE) that was modified with gold nanoparticles (AuNP). A thiolated, dual DNA probe with sequences complementary to both target sequences was immobilized onto the Au-SPCE, followed by MCH to minimize nonspecific adsorption. The hybridization of the target DNA with the probe was measured using EIS, in the presence of a ferri/ferrocyanide redox solution, at varying concentrations of *f17, yaiO,* and a combination of the two. Measurements were taken over a frequency

range of 0.10 Hz–100 kHz with an applied potential of 0 V and amplitude of 0.2 V. R_{ct} increased proportionally with the increase in *yaiO* and *f17* target DNA concentrations (1×10^{-15} to 1×10^{-17} M) from 414.3 to 1034.2 Ω and from 445.7 to 1102.0 Ω, respectfully. Correlation curves of ΔR_{ct} against log [*yaiO*] and log [*f17*] resulted in correlation coefficients above 0.995 and LODs of 0.8 fM and 1.0 fM, respectively. EIS measurement of the mixed solution concentrations resulted in a linear dependency of R_{ct} with the log of target DNA concentration, R^2 of 0.992, and LOD of 1.0 fM. The multiplex nature of the biosensor was confirmed by the ability to detect both genes for *f17*-fimbriated *E. coli* and only *yaiO* for *E. coli* that don't produce the *f17* gene. The stability of the biosensor over four weeks was confirmed, and the reproducibility was demonstrated across five sensors that resulted in an RSD of 3.8%. Target DNA selectivity was exhibited against mutated single DNA strands, non-complementary DNA, and mixtures of mutated strands. This proposed multiplexed sensor overcomes drawbacks from previous technologies, such as using multiple probes with steric crowding and nonspecific interactions between the probes, using secondary labeling, and requiring signal amplification using costly enzymes (Rabti et al., 2020).

Table 2: Summary of discussed multimarker sensors. Abbreviations include: Procalcitonin (PCT), S100 calcium-binding protein β (S-100β), Low density lipoproteins (LDL), High density lipoproteins (HDL), Hemoglobin (Hb), Glycated hemoglobin (HbA1c).

6. Continuous EIS diagnostics

With the right mixture of MREs and detection methodology, continuous detection of target analytes can be achieved. EIS's ability to monitor a system without disturbing or influencing it is highly desirable for continuous sensing, as well as its ability to obtain real-time data with small sample volumes. Continuous detection of biofilm growth, which accounts for >80% of all human microbial infections, has been demonstrated by using EIS to detect the bacteria *Pseudomonas Putida*. Biofilm-related infections affect over 12 million people in the USA, causing an estimated economic burden of $6 billion a year and pose a hazard to the food industry. A continuous flow system was used to demonstrate biofilm growth over 100-fold, 1000-fold, and 10,000-fold bacterial dilutions for 12, 49, or 63 h, respectively. The EIS setup included two stainless steel 316 seamless tubes acting as the working and counter electrodes, one as the inlet and outlet respectively, where the inner surface allowed the biofilm to form. The reference electrode was a 'LowProfile' 60-mm Ag/AgCl glass electrode inserted flush between the working and counter electrode in a T shape connector, simulating an in-line detector. EIS measurements were taken at 2 h increments for 100-fold tests and at 3.5 h increments for 1000-fold and 10,000-fold tests, with three replications of each test. This method allowed an LOD of 2.4 log CFU/cm^2 due to the inner surface area of the tubing, with the detection time of this lower limit varying based upon the concentration of planktonic cells in the flow system. The R_{ct} of the sensor decreased as the biofilm grew, which could be due to attachment of charged bacterial cells and increased biofilm conductivity. Biofilm conductivity varies upon the type of bacteria, as some form conductive biofilms (such as *Geobacter sulfurreducens* and *Staphylococcus epidermidis*) while others form low conductivity biofilms (such as *Bacillus subtilis* and *Escherichia coli*) (Yang and Reyes-De-Corcuera, 2020).

Table 2
Summarizes the discussed multimarker EIS applications discussed in this review.

Analyte	Physiological Range	Detection Range	LOD	Reference
CRP	0.3–10 μg/mL	0.01–20 μg/mL	0.1 μg/mL	Tanak et al. (2019)
PCT	0.5–10 ng/mL	0.01–10 ng/mL	0.10 ng/mL	Tanak et al. (2019)
S–100β	1–10000 pg/mL	1–10000 pg/mL	–	Cardinell et al. (2019a)
NSE	0.1–16.6 ng/mL	0–25 ng/mL	–	Cardinell et al. (2019a)
LDL	100–190 mg/dL	35.78–211.22 mg/dL	1 mg/dL	Lin et al. (2017)
HDL	40–60 mg/dL	42.43–172.65 mg/dL	1 mg/dL	Lin et al. (2017)
Hb	12–17.5 g/dL	0.5–20 g/dL	–	Boonyasit et al. (2015)
HbA1c	4.6–6.4%	2.3–14%	0.19%	Boonyasit et al. (2015); Leow (2016)
E. Coli yaiO	–	1×10^{-15}-1x10^{-17} M	0.8 fM	Rabti et al. (2020)
E. Coli f17	–	1×10^{-15}-1x10^{-17} M	1.0 fM	Rabti et al. (2020)

Continuous detection has also been achieved for detecting *E. coli* O157:H7 using a microfluidic interdigitated array microelectrode detection chip and magnetic nanoparticles. Health issues due to foodborne pathogens affect an estimated 600 million people worldwide, according to the World Health Organization, and account for an estimated foodborne illness cost of $15.6 billion in the USA. The MRE of this study was an enzymatic aptamer conjugate made up of magnetic nanoparticles (MNP), biotinylated polyclonal antibodies (Pab), bacteria, aptamer, gold nanoparticles (GNP), and urease, which resulted in the MNP-Pab-bacteria-aptamer-GNP-urease complex. The gold interdigitated microelectrode array featured 25 pairs of digit fingers with a 15 μm digit width, 15 μm inter-digit space, 3 mm digit length, and 100 nm thickness. The continuous-flow system collected EIS readings every 2 s at a flow speed of 1 mL/h, which resulted in a LOD of 1.2×10^1 CFU/mL in 2 h and detection range of 1.2×10^1 CFU/mL to 1.2×10^5 CFU/mL with an R^2 of 0.95. The enzymatic aptamer complex for *E. coli* O157:H7 detection was also found to have good specificity when compared to *Salmonella typhimurium* and *Listeria monocytogenes*, with both being under 5% separation efficiency compared to *E. coli* O157:H7 >90% separation efficiency. This was caused by the magnetic separation of the *E. coli* strain through Pab binding. The addition of the *E. coli* aptamer also caused *E. coli* O157:H7 to have a higher relative change rate of impedance compared to the other non-target bacteria, further increasing the specificity of the sensor (Yao et al., 2018).

Continuous monitoring of norepinephrine (NE) as a brain injury biomarker was investigated based on faradaic impedance-time techniques. The proposed biosensor consisted of a SAM-modified GDE, conjugated with the enzyme phenylethanolamine N-methyltransferase (PNMT). The initial EIS studies were performed over a frequency range of 1 Hz–100 kHz at an amplitude of 5 mV. An NE/PNMT cofactor solution was tested for both purified and spiked rabbit whole blood over a concentration range of 1–10,000 pg/mL. Overlays of the NE/SAM solutions and the 10% whole blood samples closely resembled those of the Randles model. The purified and 10% whole blood calibration curves taken at the OBF of 371.1 Hz generated R^2 values of 0.95 and 0.82, respectively. To test the continuous aspect of the proposed biosensor, the purified NE/SAM concentration range (0–10,000 pg/mL) was analyzed using impedance-time (Z-t) at a fixed frequency of 368 Hz for 90 s. Samples were taken in 1 s intervals for two GDE sensors, resulting in an LOD of 8 pg/mL in comparison to an ELISA LOD of 10 pg/mL. Additionally, the optimal time to record the impedance was determined to be 3 s after initialization, which is comparable to commercial glucose monitors. Z-t testing was further performed as purified 500 pg/mL NE/SAM was added at particular time intervals (30, 40, 85, 145, and 325 s), with applied frequencies of 368 Hz and 321 Hz. Significant differences at the lower frequency confirm that the OBF of NE to PNMT is 368 Hz. The study exhibited the ability of this impedimetric sensor to detect NE in both purified and complex media with reproducible LODs and shows promise for continuous detection (Haselwood and la Belle, 2015).

Work by Lorestani et al. (2019) has led to the development of a continuous, regenerative, label-free, microfluidic electrochemical immunosensor, designed to work with biomarker detection from organ-on-a-chip platforms. Continuous detection capabilities were

demonstrated by detecting Interleukin-8 (IL-8), which is a common mediator of inflammatory response. The prepared sensor utilized a screen-printed gold working electrode, gold counter electrode, and a silver reference electrode for in-line monitoring using EIS. Biotinylated antibodies were immobilized on the gold working electrode through a 11-mercaptoundecanoic acid (MUA) SAM modified with EDC/NHS. IL-8 was able to be detected from 0.0001 ng/mL to 1 μg/mL with an R^2 of 0.91. The LOD was determined to be 0.08 ng/mL, which exceeds ELISA's LOD of 0.2 ng/mL. The prepared microfluidic chip regenerative system worked by performing a CV scan and chronoamperometry to remove the functionalized layers (MUA, EDC/NHS, Antibody), then reapplying these functionalizing layers and detecting the target antigen. Continuous detection of a fixed 10 ng/mL IL-8 concentration was demonstrated 6 times using this regenerative process, resulting in a semi-consistent normalized R_{ct} value across all 6 times (ranging from 2 to 2.5 R_{ct} antigen/R_{ct} media). The regenerative cycle was demonstrated up to 30 times, with no significant loss in sensitivity, demonstrating a novel approach to long-term monitoring (Lorestani et al., 2019).

The techniques of faradaic EIS and Z-t have been recently implemented into a rapid, label-free biosensor platform for prostate-specific antigen (PSA) and neuron-specific enolase (NSE) with promise in advancing continuous applications. The sensor base consisted of a functionalized working GDE, Ag/AgCl reference, and a Pt counter electrode. The respective antibodies, anti-PSA and anti-NSE, were immobilized onto the working electrode through a 16-MHDA SAM. An electrochemical analyzer was used to perform EIS over a frequency range of 1 Hz–100 kHz at a 5 mV amplitude. The two biomarkers were tested separately in the presence of a redox probe, with concentration ranges of 0 to 10×10^3 pg/mL PSA and 0 to 25×10^3 pg/mL NSE. Initial testing indicated opposite trends between the two biomarkers, where the imaginary impedance magnitude decreased with increasing PSA concentrations, but increased with increasing NSE concentrations. This could be due, in part, to the conflicting dissociation constants and antibody-antigen kinetics of the two antibodies. Further analysis to determine the OBF in terms of sensor response and correlation was performed, indicating an OBF for PSA and NSE to be 81.38 Hz and 14.36 Hz, respectively. At these frequencies, calibration curves of imaginary impedance over PSA and NSE concentrations generated R^2 values of 0.97 and 0.93, respectively. The LOD of PSA and NSE were calculated to be 28.02 and 3.95 pg/mL, respectively. Additionally, the continuous application of the proposed biosensor was investigated for PSA in complex solution using Z-t at an applied frequency of 81.38 Hz. Impedance was measured over every second for 60 s with addition of consecutively increasing PSA concentrations (10, 1000, and 10×10^3 pg/mL). Increasing PSA concentration resulted in distinct imaginary impedance magnitude decreases over the 60 s and provided a lower LOD of 15.04 pg/mL. The comparison of the frequency sweep versus the single frequency continuous measurement indicated the potential benefit of reducing interfering frequencies for analyte detection (Honikel et al., 2019).

Table 3: Summary of discussed continuous sensors. Abbreviations include: *Pseudomonas Putida* (*P. Putida*), Interleukin-8 (IL-8), Prostate-specific antigen (PSA).

Table 3
Summarizes the discussed continuous EIS applications discussed in this review.

Analyte	Detection Period	Detection Range	LOD	Reference
P. Putida	3.5 h	1×10^4-1x10^6 CFU/mL	2.4 log CFU/cm^2	Yang and Reyes-De-Corcuera (2020)
E. Coli O157: H7	2 h	1.2×10^1-1.2 $\times 10^5$ CFU/mL	1.2×10^1 CFU/mL	Yao et al. (2018)
NE	325 s	1–10000 pg/mL	8 pg/mL	Haselwood and la Belle (2015)
IL-8	30 cycles	0.0001 ng/mL - 1 μg/mL	0.08 ng/mL	Lorestani et al. (2019)
PSA	60 s	0–10 ng/mL	15.04 pg/mL	Honikel et al. (2019)

7. Conclusion

EIS is a rapidly growing field expected to continuously advance in the next decade and has already demonstrated the fluidity necessary to be applicable to a large variety of biosensors. Recent advancements have shown EIS's ability to be used in a wide array of implementations, ranging from POC devices for single marker, continuous sensing, and multimarker detection. While its application to multimarker and continuous detection is in the early stages, interest and continued development will further evolve its untapped potential. Integration of novel MRE's, such as aptamers and artificial binding proteins, can provide further improvements for sensing a wider range of analytes. EIS sensors allow non-invasive methods of diagnostics through wearable technology, boasting both cost efficiency and user friendliness. EIS biosensors show promise in the medical industry in a variety of disciplines including, but not limited to, diabetes, cardiovascular diseases, sepsis, and cancer. This technology also provides POC features which can be used for on-site detection, which is beneficial for the medical, agricultural, and environmental monitoring fields. The technology offers biological environment preservation, along with thermal and temporal stability. There are also promising applications for heightening biosensor specificity and sensitivity through the use of hybrid and metal nanoparticles, along with carbon-based nanotubes. New opportunities for sensor base property/structure control are offered from molecularly imprinted polymers and nanostructured polymers. EIS also offers efficient experimental time and produces a large amount of useable data. The future advancements of EIS technology could enable extremely rapid and improved detection devices.

Author contributions section

All authors contributed equally as in the order presented in the authors listing in the work.

Declaration of competing interest

There are no declarations of interest to note.

References

Acero Sánchez, J.L., Fragoso, A., Joda, H., Suárez, G., McNeil, C.J., O'Sullivan, C.K., 2016. Anal. Bioanal. Chem. 408, 5337–5346. https://doi.org/10.1007/s00216-016-9630-9.
Adamson, T.L., Cook, C.B., LaBelle, J.T., 2014. J. Diabetes Sci. Technol. 8, 350–355. https://doi.org/10.1177/1932296814523874.
Ahmed, A., Rushworth, J.v., Hirst, N.A., Millner, P.A., 2014. Clin. Microbiol. Rev. 27, 631–646. https://doi.org/10.1128/CMR.00120-13.
Barnes, T.M., van de Lagemaat, J., Levi, D., Rumbles, G., Coutts, T.J., Weeks, C.L., Britz, D.A., Levitsky, I., Peltola, J., Glatkowski, P., 2007. Phys. Rev. B: Condenser 75, 23. https://doi.org/10.1103/PhysRevB.75.235410.
Bazin, I., Tria, S.A., Hayat, A., Marty, J.L., 2017. Biosens. Bioelectron. 87, 285–298. https://doi.org/10.1016/j.bios.2016.06.083.
Bhalla, N., Jolly, P., Formisano, N., Estrela, P., 2016. Essays Biochem. 60, 1–8. https://doi.org/10.1042/EBC20150001.
Bhardwaj, N., Bhardwaj, S.K., Mehta, J., Mohanta, G.C., Deep, A., 2016. Anal. Biochem. 505, 18–25. https://doi.org/10.1016/j.ab.2016.04.008.
Bhavsar, K., Fairchild, A., Alonas, E., Bishop, D.K., la Belle, J.T., Sweeney, J., Alford, T.L., Joshi, L., 2009. Biosens. Bioelectron. 25, 506–509. https://doi.org/10.1016/j.bios.2009.07.017.
Boonyasit, Y., Heiskanen, A., Chailapakul, O., Laiwattanapaisal, W., 2015. Anal. Bioanal. Chem. 407, 5287–5297. https://doi.org/10.1007/s00216-015-8680-8.
Cai, K., Tu, W., Liu, Y., Li, T., Wang, H., 2015. Sci Rep-UK. 5, 1–10. https://doi.org/10.1038/srep17479.
Campuzano, S., Yáñez-Sedeño, P., Pingarrón, J.M., 2019. Nanomaterials-basel 9 (4), 634. https://doi.org/10.3390/nano9040634.
Cardinell, B.A., Addington, C.P., Stabenfeldt, S.E., la Belle, J.T., 2019a. Crit. Rev. Biomed. Eng. 47 (3), 193–206. https://doi.org/10.1615/CritRevBiomedEng.2019026108.

Cardinell, B.A., Spano, M.L., la Belle, J.T., 2019b. Crit. Rev. Biomed. Eng. 47 (3), 207–215. https://doi.org/10.1615/CritRevBiomedEng.2019026109.
Cotta, M.A., 2020. ACS Appl. Nano Mater. 3 (6), 4920–4924. https://doi.org/10.1021/acsanm.0c01386.
Deng, A., Matloff, D., Lin, C.-E., Probst, D., Broniak, T., Alsuwailem, M., Belle, J. la, 2019. Crit. Rev. Biomed. Eng. 47 (2), 169–178. https://doi.org/10.1615/CritRevBiomedEng.2019026532.
Dinshaw, I.J., Muniandy, S., Teh, S.J., Ibrahim, F., Leo, B.F., Thong, K.L., 2017. J. Electroanal. Chem. 806, 88–96. https://doi.org/10.1016/j.jelechem.2017.10.054.
Fairchild, A.B., McAferty, K., Demirok, U.K., la Belle, J.T., 2009. IEEE/ICME. https://doi.org/10.1109/ICCME.2009.4906678.
Farzadfard, A., Shayeh, J.S., Habibi-Rezaei, M., Omidi, M., 2020. Talanta 211, 120722. https://doi.org/10.1016/j.talanta.2020.120722.
Ferri, S., Kojima, K., Sode, K., 2011. J. Diabetes Sci. Technol. 1 5 (5), 1068–1076. https://doi.org/10.1177/193229681100500507.
Gonzalez, S.I., la Belle, J.T., 2012. Biosens. J. 1, 1–5. https://doi.org/10.4303/bj/235493.
Gupta, S., Kakkar, V., 2019. Tuberculosis 118, 101852. https://doi.org/10.1016/j.tube.2019.07.003.
Haselwood, B.A., la Belle, J.T., 2015. Biosens. Bioelectron. 67, 752–756. https://doi.org/10.1016/j.bios.2014.09.032.
Hayden, A., Lin, M., Park, S., Pudek, M., Schneider, M., Jordan, M.B., Mattman, A., Chen, L.Y.C., 2017. Blood Adv. 1, 2529–2534. https://doi.org/10.1182/bloodadvances.2017012310.
He, Z., Mansfeld, F., 2009. Energy Environ. Sci. 2, 215–219. https://doi.org/10.1039/b814914c.
Hong, K.L., Sooter, L.J., 2015. BioMed Res. Int. https://doi.org/10.1155/2015/419318.
Honikel, M.M., la Belle, J.T., Belle, L., 2019. Crit. Rev. Biomed. Eng. 47 (3), 217–234. https://doi.org/10.1615/CritRevBiomedEng.2019026426.
Honikel, M.M., Lin, C.-E., Probst, D., la Belle, J.T., 2018. Crit. Rev. Biomed. Eng. 46 (1), 53–82. https://doi.org/10.1615/CritRevBiomedEng.2018025818.
Huang, J., 2018. Electrochim. Acta 281, 170–188. https://doi.org/10.1016/j.electacta.2018.05.136.
Hussain, S., Afzal, N., Profile, S., Javaid, K., 2006. Level of Interferon gamma in the blood of tuberculosis patients, 54 (1), 17–21.
Hwang, H.J., Ryu, M.Y., Park, C.Y., Ahn, J., Park, H.G., Choi, C., Ha, S. do, Park, T.J., Park, J.P., 2017. Biosens. Bioelectron. 87, 164–170. https://doi.org/10.1016/j.bios.2016.08.031.
Ito, Y., Okuda-Shimazaki, J., Tsugawa, W., Loew, N., Shitanda, I., Lin, C.E., la Belle, J., Sode, K., 2019. Biosens. Bioelectron. 129, 189–197. https://doi.org/10.1016/j.bios.2019.01.018.
Jany, P.L., Agosta, G.E., Benko, W.S., Eickhoff, J.C., Keller, S.R., Köehler, W., Koeller, D., Mar, S., Naidu, S., Ness, J.M., Pareyson, D., Renaud, D.L., Salsano, E., Schiffmann, R., Simon, J., Vanderver, A., Eichler, F., van der Knaap, M.S., Messing, A., 2015. eNeuro 2 2 (5), 1–11. https://doi.org/10.1523/ENEURO.0080-15.2015.
Khan, R., Andreescu, S., 2020. Sensors 20 (18), 5434. https://doi.org/10.3390/s20185434.
Khanwalker, M., Johns, J., Honikel, M.M., Smith, V., Maxwell, S., Santhanaraman, S., Jeffrey, Belle, L., 2019. Crit. Rev. Biomed. Eng. 47 (3), 235–247. https://doi.org/10.1615/CritRevBiomedEng.2019026545.
Killar, L.M., Eisenstein, T.K., Stocker, B.A.D., 1986. Infect. Immun. 52 (2), 504–508.
la Belle, J.T., Gerlach, J.Q., Svarovsky, S., Joshi, L., 2007. Anal. Chem. 79, 6959–6964. https://doi.org/10.1021/ac070651e.
Lan, L., Chen, D., Yao, Y., Peng, X., Wu, J., Li, Y., Ping, J., Ying, Y., 2018. ACS Appl. Mater. Interfaces 10, 42009–42017. https://doi.org/10.1021/acsami.8b15677.
Laurentius, L.B., Owens, N.A., Park, J., Crawford, A.C., Porter, M.D., 2016. Expert Rev. Mol. Molecular Diagn. 8, 883–895. https://doi.org/10.1080/14737159.2016.1205489.
Leow, M.K.S., 2016. Glycated hemoglobin (HbA1c). Acta Inf. Med. 24, 233–238. https://doi.org/10.5455/aim.2016.24.233-238.
Leva-Bueno, J., Peyman, S.A., Millner, P.A., 2020. Med. Microbiol. Immunol. 209, 343–362. https://doi.org/10.1007/s00430-020-00668-0.
Lin, C., Ryder, L., Probst, D., Caplan, M., Spano, M., LaBelle, J., 2017. Biosens. Bioelectron. 89, 743–749. https://doi.org/10.1016/j.bios.2016.10.073.
Liu, J., Jiang, X., Zhang, R., Zhang, Y., Wu, L., Lu, W., Li, J., Li, Y., Zhang, H., 2019. Adv. Funct. Mater. 29 (6), 1807326. https://doi.org/10.1002/adfm.201807326.
Löfblom, J., Feldwisch, J., Tolmachev, V., Carlsson, J., Ståhl, S., Frejd, F.Y., 2010. FEBS Lett. 548 (12), 2670–2680. https://doi.org/10.1016/j.febslet.2010.04.014.
Lorestani, F., Khademhosseini, A., Dokmeci, M.R., 2019. IEEE 1036–1039.
Loveday, D., Peterson, P., Rodgers, B., 2004. J. Coating Technol. 8, 46–52.
MacDonald, D.D., 2006. Electrochim. Acta 51 (8–9), 1376–1388. https://doi.org/10.1016/j.electacta.2005.02.107.
Mahajan, V.S., Jarolim, P., 2011. Circulation 124, 2350–2354. https://doi.org/10.1161/CIRCULATIONAHA.111.023697.
Malkoc, A., Probst, D., Lin, C., Khanwalker, M., Beck, C., Cook, C.B., la Belle, J.T., 2017. J. Diabetes Sci. Technol. 11, 930–935. https://doi.org/10.1177/1932296817699639.
McKeague, M., Derosa, M.C., 2012. J. Nucleic Acids. https://doi.org/10.1155/2012/748913.
Nara, H., Yokoshima, T., Osaka, T., 2020. Curr. Opin. Electrochem. 20, 66–77. https://doi.org/10.1016/j.coelec.2020.02.026.
Nguyen, H.H., Kim, M., 2017. Appl. Sci. Convergence Technol. 26, 157–163. https://doi.org/10.5757/asct.2017.26.6.157.
Pan, Dipanjan, Khan, M.S., Misra, S.K., Wang, Z., Daza, E., Schwartz-Duval, A.S., Kus, J. M., Pan, Debanjan, 2017. Anal. Chem. 89, 2107–2115. https://doi.org/10.1021/acs.analchem.6b04769.
Park, J.W., Jin Lee, S., Choi, E.J., Kim, J., Song, J.Y., Bock Gu, M., 2014. Biosens. Bioelectron. 51, 324–329. https://doi.org/10.1016/j.bios.2013.07.052.
Park, S.-M., Yoo, J.-S., 2003. Anal. Chem. 75, 455–461.
Rabti, A., Zayani, R., Meftah, M., Salhi, I., Raouafi, N., 2020. Microchim. Acta 187 (11), 635.
Ramírez, N., Regueiro, A., Arias, O., Contreras, R., 2009. Biotecnol. Apl. 26, 72–78.
Randviir, E.P., Banks, C.E., 2013. Anal. Methods. 5, 1098–1115. https://doi.org/10.1039/c3ay26476a.
Ravalli, A., da Rocha, C.G., Yamanaka, H., Marrazza, G., 2015. Bioelectrochemistry 106, 268–275. https://doi.org/10.1016/j.bioelechem.2015.07.010.
Sandulescu, R., Tertis, M., Cristea, C., Bodoki, E., 2015. Biosens. – Micro Nano Appl. InTech. https://doi.org/10.5772/60510.
Santos, L., Martin, P., Ghilane, J., Lacaze, P.C., Randriamahazaka, H., Abrantes, L.M., Lacroix, J.C., 2010. Electrochem. Commun. 12, 872–875. https://doi.org/10.1016/j.elecom.2010.04.008.
Sarris, A., Kliche, K., Pethambaram, P., Preti, A., Tucker, S., Jackow, C., Messina, O., Pugh, W., Hagemeister, F.B., McLaughlin, P., Rodriguez, M.A., Romaguera, J., Fritsche, H., Witzig, T., Duvic, M., Andreeff, M., Cabanillas, F., 1999. Ann Oncol 10 (4), 433–440. https://doi.org/10.1023/a:1008301602785.
Sedki, M., Chen, X., Chen, C., Ge, X., Mulchandani, A., 2020. Biosens. Bioelectron. 148, 111794. https://doi.org/10.1016/j.bios.2019.111794.
Sha, F., Salzman, G., Gupta, A., Koide, S., 2017. Protein Sci. 26 (5), 910–924. https://doi.org/10.1002/pro.3148.
Shahrokhian, S., Salimian, R., 2018. Sens. Actuators, A A. 266, 160–169. https://doi.org/10.1016/j.snb.2018.03.120.
Sharma, P.S., Pietrzyk-Le, A., D'Souza, F., Kutner, W., 2012. Anal. Bioanal. Chem. 402, 3177–3204. https://doi.org/10.1007/s00216-011-5696-6.
Shi, P., Zhang, Y., Yu, Z., Zhang, S., 2017. Sci. Rep. 7, 6500. https://doi.org/10.1038/s41598-017-06858-w.
Singh, N., Ali, M.A., Rai, P., Sharma, A., Malhotra, B.D., John, R., 2017. ACS Appl. Mater. Interfaces 9, 33576–33588. https://doi.org/10.1021/acsami.7b07590.
Stern, L.A., Case, B.A., Hackel, B.J., 2013. Curr. Opin. Chem. Eng. 2 (4), 425–432. https://doi.org/10.1016/j.coche.2013.08.009.
Tanak, A.S., Jagannath, B., Tamrakar, Y., Muthukumar, S., Prasad, S., 2019. Anal. Chim. Acta X. 3, 100029. https://doi.org/10.1016/j.acax.2019.100029.
Tertis, M., Florea, A., Sandulescu, R., Cristea, C., 2013. Sensors 13, 4841–4854. https://doi.org/10.3390/s130404841.
Thangsunan, P., Lal, N., Tiede, C., Moul, S., Robinson, J.I., Knowles, M.A., Stockley, P.G., Beales, P.A., Tomlinson, D.C., McPherson, M.J., Millner, P.A., 2021. Sens. Actuators, B 326, 128829. https://doi.org/10.1016/j.snb.2020.128829.
Waleed Shinwari, M., Zhitomirsky, D., Deen, I.A., Selvaganapathy, P.R., Jamal Deen, M., Landheer, D., 2010. Sensors 10 (3), 1679–1715. https://doi.org/10.3390/s100301679.
Wan, J., Ai, J., Zhang, Y., Geng, X., Gao, Q., Cheng, Z., 2016. Sci. Rep. 6, 19806. https://doi.org/10.1038/srep19806.
Wang, M., Hu, M., Liu, J., Guo, C., Peng, D., Jia, Q., He, L., Zhang, Z., Du, M., 2019. Biosens. Bioelectron. 132, 8–16. https://doi.org/10.1016/j.bios.2019.02.040.
Wen, T., Wang, R., Sotero, A., Li, Y., 2017. Sensors 17 (9). https://doi.org/10.3390/s17091973.
Xue, H., Zhao, J., Zhou, Q., Pan, D., Zhang, Yue, Zhang, Yuanjian, Shen, Y., 2019. ACS Appl. Nano Mater. 2, 1579–1588. https://doi.org/10.1021/acsanm.9b00050.
Yang, D., Reyes-De-Corcuera, J.I., 2020. Biofouling 36, 389–402. https://doi.org/10.1080/08927014.2020.1763966.
Yao, L., Wang, L., Huang, F., Cai, G., Xi, X., Lin, J., 2018. Sens. Actuators, B 259, 1013–1021. https://doi.org/10.1016/j.snb.2017.12.110.
Zhou, J., Rossi, J., 2017. Nat. Rev. Drug Discov. 16, 181–202. https://doi.org/10.1038/nrd.2016.199.